Geochemical Perspectives Letters

Revisiting K-Pg boundary with lithium isotopes: divergent marine and continental responses

C. Yang[1*], M. Neimard[2], A. Jouini[3], A.-M. Karpoff[4], G. Ravizza[5], A. Decarreau[6], D. Beaufort[6], S. Petit[6], M. Montanes[3], M.-E. Kerros[7], L. Reisberg[8], N. Vigier[3]

https://doi.org/10.7185/geochemlet.2628

Abstract

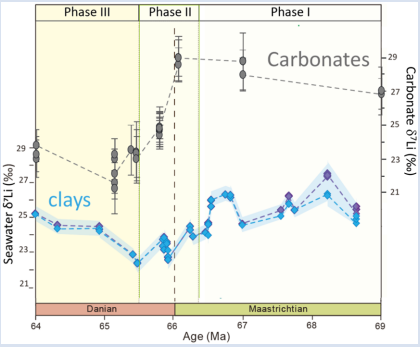

Seawater lithium isotope records (δ^7Li) are powerful tools for investigating long term climate change and its relationship with continental silicate weathering. While most past ocean δ^7Li reconstructions rely on foraminifera-rich carbonates, we introduce a novel approach using marine authigenic clays. Our findings demonstrate that clay authigenesis is an abiotic process that fractionates Li isotopes consistently in laboratory settings and across marine sediments. We apply this method to the Cretaceous-Paleogene (K-Pg) boundary, a critical interval marked by one of Earth's five largest mass extinctions, and present a new clay derived seawater δ^7Li record (64–69 Ma). Our results, compared with those of the carbonate record, uncover a dual environmental disturbance. The clay record indicates a protracted perturbation initiated at 69 Ma, driven by gradual shifts in soils, fluvial systems, and continental weathering, which remained largely unaffected by Deccan volcanism or the meteorite impact. In contrast, abrupt fluctuations are recorded in marine carbonates at 66 ± 0.3 Ma, signaling short lived yet significant changes of oceanic carbon chemistry. These findings highlight the asynchronous behaviour of terrestrial and marine systems during this major ecological transition.

Received 11 February 2026 | Accepted 12 June 2026 | Published 21 August 2026

Introduction

Reconstructing past variations in continental weathering both in rate and intensity is crucial for understanding and modelling changes in atmospheric and oceanic pCO_2 levels. Lithium isotopes (expressed as δ^7Li) in riverine and marine systems have increasingly been recognised as a robust proxy for silicate weathering intensity. Given the Li residence time in the ocean (~1.5 million years), Li isotopes are particularly well suited for investigating the global carbon cycle over extended geological periods.

Numerous studies attribute the rise in Cenozoic seawater δ^7Li values deduced from carbonates to significant changes in riverine Li flux and/or its δ^7Li composition. The riverine δ^7Li signature is primarily governed by the dissolution of silicate phases and the formation of secondary clays. A strong connection between continental silicate weathering and climate has thus been inferred from carbonate δ^7Li records (*e.g.*, Misra and Froelich, 2012; Vigier and Goddéris, 2015). On shorter time scales, such as during Oceanic Anoxic Event 2 (Pogge von Strandmann *et al.*, 2013), sedimentary carbonate records also reveal rapid δ^7Li fluctuations (≪1 Myr). These variations have been interpreted as a temperature driven acceleration of silicate weathering, subsequently impacting the carbon cycle.

At the Cretaceous-Paleogene (K-Pg) boundary (~66 Ma), δ^7Li values in foraminifera drop by ~5 ‰ in less than 400,000 years, a shift attributed to a major disruption in the marine Li budget in response to large changes in continental fluxes (Misra and Froelich, 2012). The transition from the late Maastrichtian to the Paleogene is characterised by profound environmental upheavals and one of the most devastating mass extinctions in Phanerozoic history. This catastrophic event is closely linked to two pivotal geological phenomena: the Chicxulub impact and the peak activity of the Deccan Traps volcanism (Schoene *et al.*, 2019). Both events released substantial volumes of CO_2 and SO_2 into the ocean-atmosphere system, with the impact triggering abrupt climatic shifts and the volcanism sustaining emissions over 100–150 thousand years (Schoene *et al.*, 2019; Sprain *et al.*, 2019). These processes likely induced significant changes in ocean chemistry, biogeochemical

1. State Key Laboratory of Marine Geology, Tongji University, 200092 Shanghai, China
2. Laboratoire Magmas et Volcans (LMV), Cézeaux University Campus, 63178 Aubière, France
3. Laboratoire d'Océanographie de Villefranche (LOV), IMEV, CNRS, Sorbonne Université, 06230 Villefranche-sur-Mer, France
4. Institut Terre et Environnement de Strasbourg (ITES), CNRS, Université de Strasbourg, 67084 Strasbourg, France
5. Department of Earth Sciences, University of Hawaii-Manoa, Honolulu, 96822 HI, USA
6. Institut de Chimie des Milieux et Matériaux de Poitiers (IC2MP), Université de Poitiers, 86073 Poitiers, France
7. Institute of Molecular and Cellular Pharmacology (IPMC), Université Côte d'Azur, CNRS, INSERM, France
8. Centre de Recherches Pétrographiques et Géochimiques (CRPG), CNRS, Université de Lorraine, 54500 Vandoeuvre-les-Nancy, France
* Corresponding author (email: cfyang@tongji.edu.cn)

cycles, and global environmental conditions (Henehan *et al.*, 2019). However, the precise timing and magnitude of these events, as well as their effects, remain debated.

Throughout the Phanerozoic, marine δ^7Li records have largely relied on fossil calcium carbonates, such as foraminiferal shells, dolostones, and shallow water marine carbonates (Misra and Froelich, 2012; Kalderon-Asael *et al.*, 2021; Liu *et al.*, 2023). A fundamental assumption is that they faithfully reflect the seawater δ^7Li at the time of their formation. However, biogenic carbonates represent a negligible Li sink, and biological or environmental factors may influence their δ^7Li values (Vigier *et al.*, 2015; Chen *et al.*, 2023; Poet *et al.*, 2023). In contrast, marine clays represent the dominant oceanic Li sink. Authigenic smectite can form extensively under hydrothermal or low temperature conditions, through the alteration of volcanic glass or biogenic opal (Zhao *et al.*, 2025). Marine clays are typically Li-rich compared to any other authigenic phases and they preferentially incorporate the lighter isotope (^{6}Li). This inorganic process explains the modern open ocean δ^7Li value of 31.1 ‰ ± 0.6 ‰ (Jouini *et al.*, 2026), significantly higher than that of its primary sources (riverine δ^7Li: 23 ‰; hydrothermal fluids: 8 ‰).

In this study, we explore the potential of marine clays to serve as a robust proxy for reconstructing seawater δ^7Li values at the time of their formation. We present a new high resolution δ^7Li record spanning the K-Pg transition and discuss its implications for environmental changes during this critical period.

A Single Temperature Dependent Li Isotopic Fractionation Law

To establish marine authigenic clays as reliable proxies for palaeo-seawater δ^7Li reconstruction, we first establish the seawater-clay Li isotopic fractionation factor at temperatures representative of early marine diagenesis (T < 90 °C). We then validate this approach by comparing results with modern seawater and recent carbonate shell records (0–11 Ma), a time frame particularly relevant to the long Li residence time in the ocean.

Previous experimental studies have quantified Li isotope fractionation during smectite formation at temperatures ranging from 90 °C to 250 °C, revealing significant enrichment of ^{6}Li in clays (Vigier *et al.*, 2008; Wunder *et al.*, 2010; Hindshaw *et al.*, 2019). The clay-solution Li isotopic fractionation factor is temperature dependent. However, experiments conducted below 90 °C have yielded inconclusive results. These challenges stem from lower crystallinity and the persistent presence of exchangeable Li (Vigier *et al.*, 2008). We therefore developed an optimised protocol for low temperature conditions. This protocol includes extended experiment durations to enhance crystallinity and more efficient removal of exchangeable Li, which may have a distinct isotopic composition (Yang *et al.*, 2023). Additionally, we investigated the influence of clay type and chemical composition on the fractionation factor (see the Supplementary Information for the protocol, chemical and mineralogical analyses by XRD, FTIR and TEM).

Collectively, the new and published data reveal a consistent temperature dependent trend for the clay-solution Li isotopic fractionation factor (Fig. 1). Over a range of 25 °C to 250 °C, the fractionation factor exhibits an inverse correlation with temperature, independent of solution chemistry and of the amount of Li incorporated into the crystalline structure. As a result, the δ^7Li signature of smectite is primarily governed by two key factors: (1) temperature, and (2) the δ^7Li value of the solution. This relationship provides a theoretical framework for reconstructing water δ^7Li values from clay samples. Using

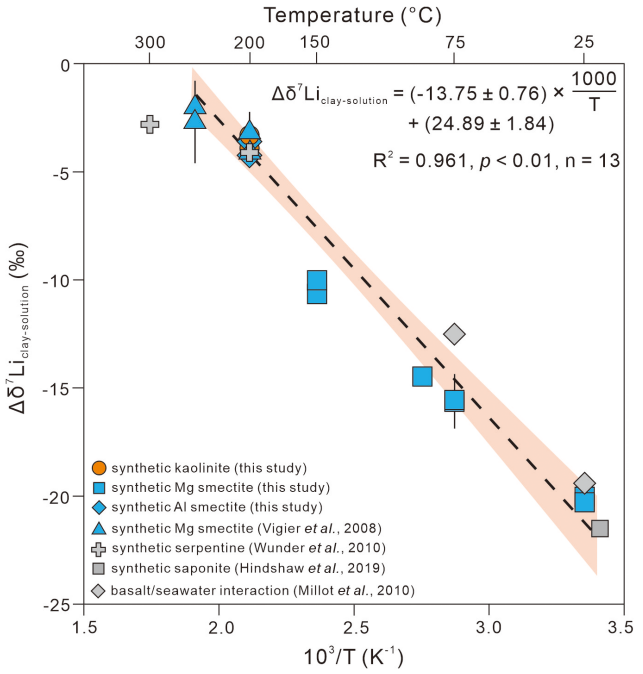

Figure 1 Temperature dependent Li isotope fractionation during clay formation ($\Delta\delta^7Li_{clay\text{-}solution} = \delta^7Li_{clay} - \delta^7Li_{solution} = 1000\ln(\alpha)$, with α denoting isotopic fractionation factor). The linear fitted line with a 95 % confidence interval is drawn based on data from synthetic smectite (blue symbols) from this study and Vigier *et al.* (2008). Data for synthetic kaolinite (this study), serpentine (grey plus), saponite (grey square), and basalt/seawater interaction (grey diamonds) are shown for comparison (Wunder *et al.*, 2010; Millot *et al.*, 2010; Hindshaw *et al.*, 2019).

weighted linear regression that accounts for analytical uncertainties, the empirical relationship derived from experimental studies can be expressed by the equation:

$$\Delta\delta^7Li_{smectite\text{-}solution} = (-13.75 \pm 0.76) \times \frac{1000}{T} + (24.89 \pm 1.84)$$

where T is in Kelvin. Although this relationship is primarily established for Mg smectite, the δ^7Li values of kaolinite and Al smectite (formed at 200 °C) with distinct chemical compositions (see Table S-1) also adhere to this trend. Additionally, published data for various secondary phases and clay mixtures are also consistent with our new experiments (Fig. 1). This unity is explained by theoretical modelling (Dupuis *et al.*, 2017), which identifies the strength of the Li-O bond and its corresponding vibrational energy as the primary factor controlling the preferential incorporation of ^{6}Li into the clay structure. The Li-O bonding dynamics can overshadow potential isotopic effects arising from variations in solution or clay chemistry. This consistent linear correlation suggests that the Li isotopic fractionation during Li incorporation into clay octahedral sites is largely independent of clay type (kaolinite or smectite) and its chemical composition. Instead, temperature emerges as the dominant control.

Authigenic Clays: a New Proxy of Past Seawater δ^7Li Variations

To assess the applicability of the relationship in Figure 1 for reconstructing palaeo-seawater δ^7Li variations, we studied smectite-rich sediments collected through international ocean drilling programmes (DSDP, ODP). These samples represent both modern (core top sediments) and "recent" (<11 Myr)

formation. Modern seawater δ^7Li values, extensively documented in the literature, are close to homogeneous (δ^7Li = 31.1 ± 0.6 ‰; Jouini *et al.*, 2026). Given the Li residence time in the ocean, seawater Li concentration and δ^7Li values can be considered stable over the past 4–5 million years. Furthermore, palaeo-environmental studies using beryllium 10 (Lenard *et al.*, 2020) also indicate steady erosion rates during the late Cenozoic, implying negligible disturbances in riverine Li flux and only minor variations in the oceanic Li budget during this period. Thus, our analysis of recent and sub-recent authigenic clays from open ocean environments provides a robust framework to verify whether the solution δ^7Li values derived from the α-T relationship in Figure 1 are valid.

The core top smectite-rich clays from Valdivia VA13/2 96BL drill core yield an average δ^7Li value of 5.6 ± 0.6 ‰ (see Table S-7). Using the equation given above and a temperature typical of the Central Pacific abyssal hill (3 °C), this corresponds to a seawater δ^7Li value of 30.5 ± 0.6 ‰ that is consistent with that of modern seawater (δ^7Li = 31.1 ± 0.6 ‰; Jouini *et al.*, 2026). Over the 0–11 Ma period, δ^7Li records from foraminifera, brachiopod, bulk carbonates and dolostones document a roughly consistent trend (Misra and Froelich, 2012; Washington *et al.*, 2020; Liu *et al.*, 2023). Note that some of these data had been corrected for isotopic vital (biological) effects during shell growth. We analysed smectite-rich marine sediments from sites 800, 1218, and 1219 in the Tropical Pacific Ocean to reconstruct seawater δ^7Li variations over the past 11 million years (see Table S-7). These samples were thoroughly characterised using scanning electron microscopy (SEM), laser ablation spectroscopy (LAS), and X-ray diffraction (XRD). Sediments with >80 % smectite content and no detectable opal or quartz were selected to minimise detrital inputs (see Supplementary Information).

Using the experimental α-T relationship (Fig. 1) and deep ocean temperature (Meckler *et al.*, 2022), we calculated the δ^7Li values of seawater in equilibrium with clays during their formation. Over the past 5 million years, smectite-rich clay fractions yield seawater δ^7Li values ranging from 29.7 ± 0.3 ‰ to 30.5 ± 0.6 ‰, consistent with the relatively stable values observed in carbonate records (Fig. 2). From 5 to 10.6 million years ago, clay derived δ^7Li values gradually decline to 28.1 ± 0.5 ‰, a trend that matches the general pattern established from carbonates. Deep sea water temperature reconstructions for this period may carry an uncertainty of 3–8 °C (Meckler *et al.*, 2022). Considering this, the propagated uncertainty for seawater δ^7Li values reconstructed from marine authigenic clays is ~1.1 ‰ (see Supplementary Information). Additionally, uncertainty may arise from structural differences between the natural and experimentally synthesised clays. The time scale of authigenic clay formation in the deep sea has recently been constrained to <40 days (Zhao *et al.*, 2025), which is close to our synthesis times at low temperatures. The faster reaction rates typically result in the formation of less crystalline minerals. Nevertheless, the complete removal of exchangeable Li and the consistent $\Delta\delta^7$Li values of −20.3 ‰ and −20.0 ‰ observed at 25 °C after 4 and 8 weeks strongly suggest that Li isotopic equilibration has been achieved in our experiments (Table S-1). We acknowledge that potential differences may exist between synthetic and natural authigenic clays, and that Li isotope fractionation during natural authigenic clay formation requires further investigation.

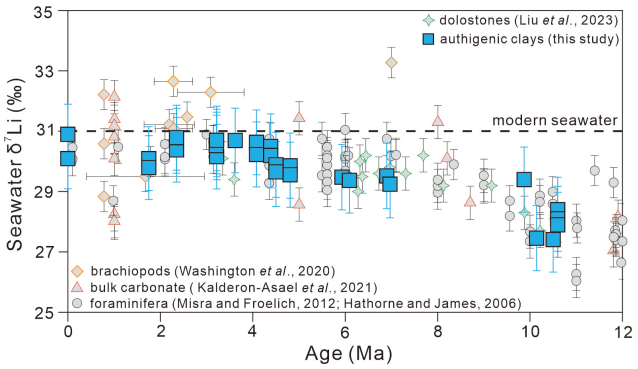

Figure 2 Record of seawater δ^7Li values over the past 11 Ma. Seawater δ^7Li values from our study are represented by blue squares. Published data for foraminifera (grey circles), brachiopods (grey diamonds with orange edges), bulk carbonate (grey triangles with red edges) and dolostones (grey stars with green edges) are shown (Hathorne and James, 2006; Misra and Froelich, 2012; Washington *et al.*, 2020; Kalderon-Asael *et al.*, 2021; Liu *et al.*, 2023).

There are advantages of using authigenic smectite-rich clays to reconstruct palaeo-oceanic δ^7Li variations. Planktonic foraminifera underwent significant biotic crises, such as observed at the Cretaceous-Paleogene (K-Pg) boundary, and the influence of vital effects on the biogenic δ^7Li values remains a subject of debate. Our clay based δ^7Li proxy opens new potentials in settings where carbonate archives are absent or ambiguous. While diagenetic effects warrant further investigation, our study indicates that their impact is minimal, likely due to the negligible influence of exchangeable Li within clays. In contrast, marine carbonates display Li concentrations several orders of magnitude lower than those in clays, suggesting that their Li isotopic compositions may be more susceptible to modification.

Ocean δ^7Li Variations across the K-Pg Boundary

During the transition from the Late Maastrichtian to the Danian, seawater δ^7Li values reconstructed from planktonic foraminifera records initially exhibit a gradual increase between 69 and 66 million years ago, followed by an abrupt and pronounced decrease of ~5 ‰ in less than 400,000 years (Fig. 3b). This rapid decline has been attributed to enhanced dissolution of continental soils and a massive increase in riverine Li flux (Misra and Froelich, 2012). However, the duration of this event is brief compared to the modern Li residence time in the ocean and the time scales required for changing the continental weathering regime. Notably, the dominance of thick lateritic soils during the Cretaceous also suggests a buffering effect against rapid changes (Vigier and Goddéris, 2015). The abrupt δ^7Li decrease in foraminifera at 66 Ma cannot be explained by a shorter oceanic Li residence time, as the expected rapid return to the preceding K-Pg values is absent. Instead, environmental disruptions like meteorite impacts or massive volcanism may have altered foraminiferal growth. For instance, temperature and pH changes can alter growth rates, which in turn affects both the entrapment of trace elements (including lithium) in crystals and the kinetics of isotopic fractionation (*e.g.*, Vigier *et al.*, 2015; Roberts *et al.*, 2018; Chen *et al.*, 2023). Species specific characteristics may have also influenced vital (isotopic) effects, as marine biodiversity underwent substantial and rapid changes during the K-Pg transition.

We reconstructed seawater δ^7Li variations using smectite-rich sediments from DSDP Site 524 in the Southwest Atlantic across the K-Pg boundary. Samples were meticulously selected based on a comprehensive analysis of their chemical and mineralogical compositions (SEM, TEM, XRD, FTIR), which consistently demonstrated the dominance of authigenic smectite and a low degree of diagenesis (see Supplementary Information). We used the ocean bottom water temperature calculated from δ^{18}O records

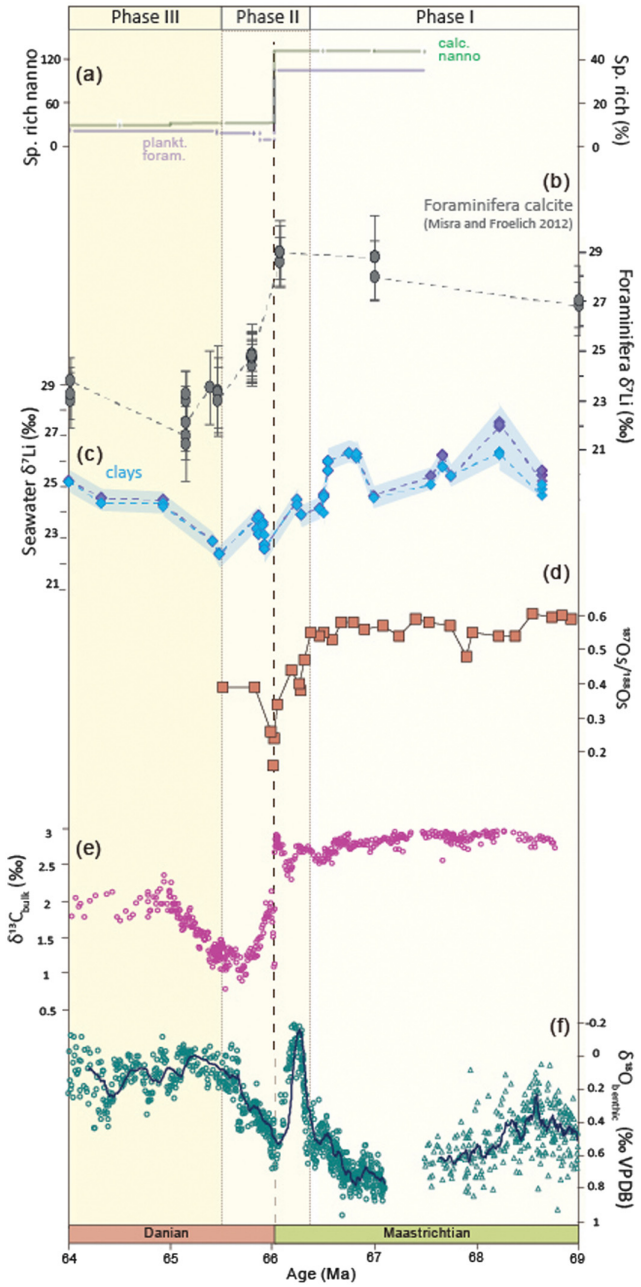

Figure 3 **(a)** Global species richness of foraminifera (pale purple) and nannofossils (green) (Hull *et al.*, 2020). **(b)** δ^7Li values of planktonic foraminifera (Misra and Froelich, 2012). **(c)** Seawater δ^7Li values reconstructed from marine clays (DSDP site 524; this study). Blue diamonds are corrected using temperatures from clumped isotopes (63–65.5 Ma; Meckler *et al.*, 2022) and bottom water δ^{18}O (65.5–68.8 Ma; Dameron *et al.*, 2017; Barnet *et al.*, 2019). Purple diamonds use bottom water δ^{18}O (63–67 Ma; Barnet *et al.*, 2019) and benthic Mg/Ca based temperatures (67–68.8 Ma; Fischer *et al.*, 2025). The shaded blue area represents external reproducibility (±0.4 ‰). **(d)** Osmium isotope record (DSDP Site 577; Ravizza and Peucker-Ehrenbrink, 2003). **(e)** Bulk carbonate δ^{13}C (IODP Site U1403; Hull *et al.*, 2020). **(f)** Benthic foraminiferal δ^{18}O records from IODP Site 1262 (green circles; Barnet *et al.*, 2019) and U1403 (green triangles; Fischer *et al.*, 2025). The K-Pg boundary is marked by a dashed line at 66.043 ± 0.040 Ma.

from the Atlantic Ocean and from Mg/Ca ratios of benthic foraminifera (Hull *et al.*, 2020; Fischer *et al.*, 2025).

From 69 to 64 million years ago, the clay derived seawater δ^7Li record can be divided into three distinct phases (Phases I, II, and III in Fig. 3). During Phase I (69–66.5 Ma), the seawater δ^7Li trend closely follows the benthic foraminifera δ^{18}O record, suggesting that the surface Li cycle was influenced by temperature. This phase is characterised by an initial increase in δ^7Li, followed by a gradual decline over 2 million years. Phase II (66.5–65.5 Ma) coincides with the peak of Deccan volcanism, as well as the Ir-rich layer and the osmium isotope decline, which are often interpreted as evidence of the Chicxulub impact (though this remains debated). This period also includes rapid and pronounced δ^{18}O fluctuations. Recent studies indicate that the main phase of Deccan volcanism lasted ~1 million years and can be further divided into four distinct mega-pulses (*e.g.*, ~66.1–66.0 Ma and ~65.9–65.8 Ma; Schoene *et al.*, 2019; Sprain *et al.* 2019). Despite these volcanic and impact related events, seawater δ^7Li derived from the clay record remains low, and only small variations are observed throughout this interval (Fig. 3). Finally, in Phase III (65.5–64 Ma), following the cessation of major Deccan volcanic activity, clay data show that the seawater δ^7Li value gradually returns to its mid-Maastrichtian level (~25 ‰).

During Phase I (69–66.5 Ma), the parallel trends in δ^{18}O and δ^7Li records suggest a long term climatic influence on continental silicate weathering, likely due to progressive soil evolution (*e.g.*, Vigier and Goddéris, 2015). Fischer *et al.* (2025) attributed the temperature decline after 68.5 Ma to reduced CO_2 levels linked to variations in continental weathering and volcanic activity. They consider that Ninetyeast Ridge volcanism triggered a warming event at ~69.2 Ma and the Mid-Maastrichtian Event, followed by cooling due to enhanced silicate weathering. The decrease in seawater δ^7Li aligns with this interpretation.

In Phase II (66.5–65.5 Ma), clay derived seawater δ^7Li reaches its lowest values with minimal fluctuation, indicating that the Deccan Traps volcanic pulses and the Chicxulub impact did not significantly perturb the riverine flux and the marine Li budget. Conversely, planktonic foraminifera exhibit a sharp δ^7Li decline (~5 ‰), likely due to vital effects influenced by changes in dissolved inorganic carbon (DIC) or pH (Vigier *et al.*, 2015; Roberts *et al.*, 2018; Poet *et al.*, 2023). Supporting this, calcium isotopes reveal significant $\delta^{44/40}$Ca fluctuations in foraminifera at the K-Pg boundary (Jouini *et al.*, 2023), tied to disruptions in ocean carbonate chemistry (CO_3^{2-}, DIC, Ω) and associated biological responses. Boron isotopes also demonstrate a rapid increase in seawater pH by ~0.4 units after the K-Pg boundary (Henehan *et al.*, 2019). Based on the proposed pH-δ^7Li relationship (Roberts *et al.*, 2018), this change is sufficient to drive the observed δ^7Li decline in foraminifera.

Overall, these findings highlight the asynchronous behaviour of terrestrial and marine systems during this major ecological transition. The contrasting records between clays and foraminifera illustrate the role of long term climate change on continental weathering. At the boundary, rapid changes in carbonates δ^7Li are consistent with large atmospheric carbon fluctuations profoundly impacting calcifier biology, with minimal impact on continental fluxes.

Acknowledgements

This work was funded by CNRS-INSU SYSTER, by the ANR INTOCC (Grant No. ANR-15-CE31-0013), and by the National Natural Science Foundation of China (Grant No. 42376057). AJ is funded by the ERC Advanced "SeaLi2Bio" (Grant #101097738). Many thanks to Bremen Core Collection team for access to Deep Sea Core Samples, to Ken Rubin, Denys Vonderhaar and Doug Pyle from Hawaii University, to Pierre Chansigaud from IC2MP for FTIR measurements, and to Philippe Telouk at CNRS-INSU national service (ENS-Lyon). We would like to thank

the anonymous reviewer and Xiao-Ming Liu for their constructive comments, which have enhanced the quality of this manuscript.

Editor: Gavin Foster

Additional Information

Supplementary Information accompanies this letter at https://www.geochemicalperspectivesletters.org/article2628.

Cite this letter as: Yang, C., Neimard, M., Jouini, A., Karpoff, A.-M., Ravizza, G., Decarreau, A., Beaufort, D., Petit, S., Montanes, M., Kerros, M.-E., Reisberg, L., Vigier, N. (2026) Revisiting K-Pg boundary with lithium isotopes: divergent marine and continental responses. *Geochem. Persp. Let.* 41, 24–28. https://doi.org/10.7185/geochemlet.2628

References

Barnet, J.S.K., Littler, K., Westerhold, T., Kroon, D., Leng, M.J., Bailey, I., Röhl, U., Zachos, J.C. (2019) A High-Fidelity Benthic Stable Isotope Record of Late Cretaceous–Early Eocene Climate Change and Carbon-Cycling. *Paleoceanography and Paleoclimatology* 34, 672–691. https://doi.org/10.1029/2019PA003556

Chen, D., Thibon, F., Felbacq, A., Weppe, L., Metian, M., Vigier, N. (2023) Coupled survey of lithium isotopes and Li/Ca in biogenic and inorganic carbonates. *Earth-Science Reviews* 244, 104500. https://doi.org/10.1016/j.earscirev.2023.104500

Dameron, S.N., Leckie, R.M., Clark, K., MacLeod, K.G., Thomas, D.J., Lees, J.A. (2017) Extinction, dissolution, and possible ocean acidification prior to the Cretaceous/Paleogene (K/Pg) boundary in the tropical Pacific. *Palaeogeography, Palaeoclimatology, Palaeoecology* 485, 433–454. https://doi.org/10.1016/j.palaeo.2017.06.032

Dupuis, R., Benoit, M., Tuckerman, M.E., Meheut, M. (2017) Importance of a Fully Anharmonic Treatment of Equilibrium Isotope Fractionation Properties of Dissolved Ionic Species As Evidenced by Li^+(aq). *Accounts of Chemical Research* 50, 1597–1605. https://doi.org/10.1021/acs.accounts.6b00607

Fischer, A., Batenburg, S.J., Bahr, A., Voigt, S., Rheinberger, A., Schmickal, S., Rheinberger, S., Greule, M., Rheinberger, S., Friedrich, O. (2025) Precession-paced late Maastrichtian bottom-water dynamics. *Communications Earth & Environment* 6, 239. https://doi.org/10.1038/s43247-025-02219-y

Hathorne, E.C., James, R.H. (2006) Temporal record of lithium in seawater: A tracer for silicate weathering? *Earth and Planetary Science Letters* 246, 393–406. https://doi.org/10.1016/j.epsl.2006.04.020

Henehan, M.J., Ridgwell, A., Thomas, E., Zhang, S., Alegret, L., *et al.* (2019) Rapid ocean acidification and protracted Earth system recovery followed the end-Cretaceous Chicxulub impact. *Proceedings of the National Academy of Sciences* 116, 22500–22504. https://doi.org/10.1073/pnas.1905989116

Hindshaw, R.S., Tosca, R., Gout, T.L., Farnan, I., Tosca, N.J., Tipper, E.T. (2019) Experimental constraints on Li isotope fractionation during clay formation. *Geochimica et Cosmochimica Acta* 250, 219–237. https://doi.org/10.1016/j.gca.2019.02.015

Hull, P.M., Bornemann, A., Penman, D.E., Henehan, M.J., Norris, R.D., *et al.* (2020) On impact and volcanism across the Cretaceous-Paleogene boundary. *Science* 367, 266–272. https://doi.org/10.1126/science.aay5055

Jouini, A., Paris, G., Caro, G., Bartolini, A., Gardin, S. (2023) Constraining oceanic carbonate chemistry evolution during the Cretaceous-Paleogene transition: Combined benthic and planktonic calcium isotope records from the equatorial Pacific Ocean. *Earth and Planetary Science Letters* 619, 118305. https://doi.org/10.1016/j.epsl.2023.118305

Jouini, A., Payant, L., Vigier, N. (2026) Advances in high-precision lithium isotopic measurements with the Neoma™ MC-ICP-MS. *Journal of Analytical Atomic Spectrometry* 41, 1004–1016. https://doi.org/10.1039/D5JA00426H

Kalderon-Asael, B., Katchinoff, J.A.R., Planavsky, N.J., Hood, A.V.S., Dellinger, M., *et al.* (2021) A lithium-isotope perspective on the evolution of carbon and silicon cycles. *Nature* 595, 394–398. https://doi.org/10.1038/s41586-021-03612-1

Lenard, S.J.P., Lavé, J.M., France-Lanord, C., Aumaître, G., Bourlès, D.L., Keddadouche, K. (2020) Steady erosion rates in the Himalayas through late Cenozoic climatic changes. *Nature Geoscience* 13, 448–452. https://doi.org/10.1038/s41561-020-0585-2

Liu, X.-F., Liu, X.-M., Wang, X.-K., Zhai, S., Liu, X. (2023) Dolostone as a reliable tracer of seawater lithium isotope composition. *Communications Earth & Environment* 4, 58. https://doi.org/10.1038/s43247-023-00711-x

Meckler, A.N., Sexton, P.F., Piasecki, A.M., Leutert, T.J., Marquardt, J., *et al.* (2022) Cenozoic evolution of deep ocean temperature from clumped isotope thermometry. *Science* 377, 86–90. https://doi.org/10.1126/science.abk0604

Millot, R., Scaillet, B., Sanjuan, B. (2010) Lithium isotopes in island arc geothermal systems: Guadeloupe, Martinique (French West Indies) and experimental approach. *Geochimica et Cosmochimica Acta* 74, 1852–1871. https://doi.org/10.1016/j.gca.2009.12.007

Misra, S., Froelich, P.N. (2012) Lithium isotope history of Cenozoic seawater: changes in silicate weathering and reverse weathering. *Science* 335, 818–823. https://doi.org/10.1126/science.1214697

Poet, M., Vigier, N., Bouret, Y., Jarretou, G., Gautier, R., *et al.* (2023) Biological fractionation of lithium isotopes by cellular Na^+/H^+ exchangers unravels fundamental transport mechanisms. *iScience* 26, 106887. https://doi.org/10.1016/j.isci.2023.106887

Pogge von Strandmann, P.A.E., Jenkyns, H.C., Woodfine, R.G. (2013) Lithium isotope evidence for enhanced weathering during Oceanic Anoxic Event 2. *Nature Geoscience* 6, 668–672. https://doi.org/10.1038/ngeo1875

Ravizza, G., Peucker-Ehrenbrink, B. (2003) Chemostratigraphic Evidence of Deccan Volcanism from the Marine Osmium Isotope Record. *Science* 302, 1392–1395. https://doi.org/10.1126/science.1089209

Roberts, J., Kaczmarek, K., Langer, G., Skinner, L.C., Bijma, J., Bradbury, H., Turchyn, A.V., Lamy, F., Misra, S. (2018) Lithium isotopic composition of benthic foraminifera: A new proxy for paleo-pH reconstruction. *Geochimica et Cosmochimica Acta* 236, 336–350. https://doi.org/10.1016/j.gca.2018.02.038

Schoene, B., Eddy, M.P., Samperton, K.M., Keller, C.B., Keller, G., Adatte, T., Khadri, S.F.R. (2019) U-Pb constraints on pulsed eruption of the Deccan Traps across the end-Cretaceous mass extinction. *Science* 363, 862–866. https://doi.org/10.1126/science.aau2422

Sprain, C.J., Renne, P.R., Vanderkluysen, L., Pande, K., Self, S., Mittal, T. (2019) The eruptive tempo of Deccan volcanism in relation to the Cretaceous-Paleogene boundary. *Science* 363, 866–870. https://doi.org/10.1126/science.aav1446

Vigier, N., Goddéris, Y. (2015) A new approach for modeling Cenozoic oceanic lithium isotope paleo-variations: the key role of climate. *Climate of the Past* 11, 635–645. https://doi.org/10.5194/cp-11-635-2015

Vigier, N., Decarreau, A., Millot, R., Carignan, J., Petit, S., France-Lanord, C. (2008) Quantifying Li isotope fractionation during smectite formation and implications for the Li cycle. *Geochimica et Cosmochimica Acta* 72, 780–792. https://doi.org/10.1016/j.gca.2007.11.011

Vigier, N., Rollion-Bard, C., Levenson, Y., Erez, J. (2015) Lithium isotopes in foraminifera shells as a novel proxy for the ocean dissolved inorganic carbon (DIC). *Comptes Rendus. Géoscience* 347, 43–51. https://doi.org/10.1016/j.crte.2014.12.001

Washington, K.E., West, A.J., Kalderon-Asael, B., Katchinoff, J.A.R., Stevenson, E.I., Planavsky, N.J. (2020) Lithium isotope composition of modern and fossilized Cenozoic brachiopods. *Geology* 48, 1058–1061. https://doi.org/10.1130/G47558.1

Wunder, B., Deschamps, F., Watenphul, A., Guillot, S., Meixner, A., Romer, R.L., Wirth, R. (2010) The effect of chrysotile nanotubes on the serpentine-fluid Li-isotopic fractionation. *Contributions to Mineralogy and Petrology* 159, 781–790. https://doi.org/10.1007/s00410-009-0454-x

Yang, C., Yang, S., Vigier, N. (2023) Li isotopic variations of particulate non-silicate phases during estuarine water mixing. *Geochimica et Cosmochimica Acta* 354, 229–239. https://doi.org/10.1016/j.gca.2023.06.020

Zhao, S., Saad, E.M., Pickering, R.A., Liu, P., Zuo, H., *et al.* (2025) Rapid transformation of biogenic silica to authigenic clay: Mechanisms and geochemical constraints. *Science Advances* 11, eadt3374. https://doi.org/10.1126/sciadv.adt3374

Revisiting K-Pg boundary with lithium isotopes: divergent marine and continental responses

C. Yang, M. Neimard, A. Jouini, A.M. Karpoff, G. Ravizza, A. Decarreau, D. Beaufort, S. Petit, M. Montanes, M.E. Kerros, L. Reisberg, N. Vigier

Supplementary Information

The Supplementary Information includes:

This Supplementary Information contains five sections, 9 tables, and 9 figures, which present the experimental protocols for clay synthesis and Li adsorption/saturation, the description of marine sampling sites and Li isotope measurements, and the mineralogical and crystal-chemical characterization of synthetic and marine clays, including XRD, FTIR, SEM/TEM observations, isotopic data, and the age model for Site 524.

1. Smectite and Kaolinite Synthesis

In smectite crystals, lithium (Li) occupies different sites: Li^+ substituting for Mg^{2+} in the structural octahedral sites (referred to as "structural Li"), and exchangeable Li^+ in the interlayer position, which compensates for the negative layer charge resulting from the Li^+-Mg^{2+} hetero-valent substitution process. Vigier *et al.* (2008) experimentally determined the Li isotope fractionation associated with the Li-Mg substitution process at various temperatures (ranging from 25 °C to 250 °C) using methods similar to those used here. A negative correlation between δ^7Li and temperature was observed between 250 °C and 90 °C. However, below 90 °C, the Li isotopic fractionation remained relatively constant as a function of temperature. X-ray diffraction (XRD) measurements revealed a low degree of crystallinity in clays synthesized below 90 °C, with a non-negligible fraction of distorted (characterized by varying interatomic distances) octahedra in the final solids.

For this study, we optimized the protocol for smectite synthesis at 25 °C, 75 °C, 90 °C, and 150 °C to improve the determination of Li isotope fractionation at these temperatures and minimize the presence of Li^+ ions located in distorted (weakly crystallized) octahedral sites, which may exhibit distinct isotopic signatures due to differences in vibrational energies. To achieve this, we increased the degree of solid crystallinity by extending the experiment duration and more effectively removed exchangeable Li using the method described below.

In brief, the synthesis of Mg-Li smectite involves a hydrothermal treatment of a starting material in a closed system (as published in Decarreau, 1980, 1983, 1985). The synthesis process begins with the formation of a silico-metallic gel with a high specific surface area, achieved by mixing sodium silicate ($SiO_2 \cdot Na_2O$) with $MgCl_2$ salt:

$$4\ SiO_2Na_2O + 3\ MgCl_2 + 2\ HCl \rightarrow Si_4Mg_3O_{11},nH_2O + 8\ NaCl + H_2O \quad \text{Eq. S-1}$$

Following precipitation, the gel is recovered by filtration and gently washed with deionized water to remove sodium chloride and prevent gel dissolution. The gel is then dehydrated through lyophilization. Subsequently, 500 mg of the powdered gel is placed in contact with a LiCl solution (see Table S-1) in sealed Teflon-coated metallic bombs, which are heated at a constant temperature for several weeks. In one experiment at 25 °C (exp #1 in Table S-1), the gel is first allowed to evolve with water at 60 °C for 10 days to form stevensite before being exposed to the LiCl solution.

Highly enriched Li solutions are used to ensure that Li blanks and Li uptake by the clay during synthesis are negligible relative to the available dissolved Li. The crystal growth associated with Li incorporation can be described by the following reaction (Decarreau, 1985):

$$[Si_4Mg_3O_{10-\varepsilon}(OH)_{2+\varepsilon}]^+ + {}_{2x}Li^+ \rightarrow (Mg_{3-x}Li_x)Si_4O_{10}(OH)_2Li_x^+{}_{exch} + {}_xMg^{2+} + {}_\varepsilon H^+ \quad \text{Eq. S-2}$$

(starting gel) (hectorite)

Reaction (2), which corresponds to hectorite formation, is associated with the release of H^+ into the solution. As a consequence, the decrease in pH has been used as an indicator of crystal growth during the experiments. At high temperatures (200 °C – 250 °C), synthesis reactions were maintained for 4 weeks under equilibrium vapor pressure (as in Vigier *et al.*, 2008). In the current study, experiments conducted between 25 °C and 150 °C were continued between 4 and 16 weeks to improve the crystallinity of the final solids. The solid phases were then separated by filtration and dried overnight at 40 °C using a lyophilization technique before analysis by X-ray diffraction (XRD) and Fourier Transform Infrared Spectroscopy (FTIR).

As described above, the removal of exchangeable Li was also improved. In Vigier *et al.* (2008), a fraction of the synthesized clay was saturated three times using either a 1N NH_4Cl or a 1N $CaCl_2$ solution with a dialysis technique. This process exchanges all the Li located in the interlayer position with NH_4 or Ca, respectively. In the current study, we added an additional step in which we first exchanged Li^+ with Mg^{2+} using a 1N $MgCl_2$ solution and dialysis bags. This step was added to remove the Li^+ ions located in distorted octahedral sites, which may exchange more easily with Mg^{2+} and are not efficiently removed by NH^{4+}, which targets only the interlayer sites).

At 200 °C, Al-smectite and kaolinite were also synthesized in order to determine the effect of clay chemical composition on the Li isotope fractionation factor. For this, two gels with Al were initially prepared, according to this reaction:

$$4\ SiO_2Na_2O + x\ MgCl_2 + y\ AlCl_3 + 2\ HCl \rightarrow Si_4Mg_xAl_yO11,nH_2O + 8\ NaCl \quad \text{Eq. S-3}$$

with x and y being 0.3 and 1.8 respectively for the first set of experiments and 0.6 and 1.6 respectively for the second set (Table S-1). The gels were collected by filtration, rinsed with deionized water, and lyophilized. In both cases, 500 mg of gel was placed in contact with 30 ml of a 3M LiCl solution in an oven at 200 °C for 4 weeks. The clays collected at the end of the experiments were saturated using NH_4Cl to remove exchangeable Li^+ ions, as described above. X-ray diffraction (XRD) measurements on the final solid aliquots indicated that the dominant fraction consisted of kaolinite for the first set and Al-Mg-Li smectite mixed with about 10% of kaolinite, for the second set (unshown).

2. Li Adsorption/Saturation Experiments

In smectite, Li^{+} occurs mostly in the octahedral sites, substituting for Mg^{2+}, forming covalent bonds with O^{2-}. As a consequence, we expect that the isotopic fractionation factor determined for this process (using the method described in the previous section) to be representative. Nevertheless, part of Li^{+} may also occupy exchangeable sites of smectite. Even though prior work has shown that smectite contains only small amounts of exchangeable Li (*e.g.*, Decarreau *et al.*, 2012), we also focused our efforts to constrain the isotopic fractionation factor corresponding to Li adsorption. Li exchangeable sites are located either in the interlayer position (as a permanent positive charge balancing the smectite negative layer charge) or at the lateral edge of the layer (as a variable charge). Since the vibration energy depends on the local atomic environment and the length of the bond between Li^{+} and nearby ions, it is expected that each different site is associated with a distinct isotopic fractionation factor, both of them being strongly different from that resulting from the Li-Mg substitution process described in the previous section.

We performed Li adsorption and desorption experiments using the reference smectite SAz-1 (Montmorillonite) from the CMS source clays (Source clays – The Clay Minerals Society). SAz-1 is an Al-smectite from Apache County, Arizona, with the formula $(Si_{3.93}\ Al0_{.07})\ (Al_{1.48}\ Mg_{0.66}\ Fe^{3+}_{0.09}\ Ti_{0.01})\ O_{10}(OH)_2\ Ca_{0.44}$ (<2µm fraction) (Mermut and Cano, 2001). In these experiments, two samples of 500 mg of SAz-1 were initially placed in 40 ml of a 1M NH_4Cl solution to remove all possible residual exchangeable Li^{+} before the experiments. Then, two 300 mg aliquots of these samples were placed into a dialysis bag containing 500 ml of a 1M LiCl solution. After a few hours, the solution was collected, along with the Li-saturated SAz-1 clay. One clay aliquot (noted #1 in Table S-2) was rinsed using 10^{-4}N LiCl, and one (noted #2) was rinsed with Milli-Q water. For comparison, another aliquot of SAz-1 was saturated with calcium (noted #4).

In an attempt to distinguish the influence of the interlayer sites and the octahedral edge sites, another experiment was performed during which a Ca-SAz-1 aliquot was first saturated with Cs (using a 0.01N CsCl solution) and then with Li (using 1N LiCl). In this experiment, Cs is expected to incorporate preferentially the interlayer site (as a permanent charge), leaving most of the exchangeable Li+ to occupy the edge sites. However, as described in Table S-2, the SAz-1 Li concentration at the end of this experiment was only 20% lower compared to experiments #1 and #2, suggesting that in addition to occupying the edge sites, the Li had replaced most of the Cs in the interlayer sites as well.

3. Marine Sites

In this study, marine sediments come from deep basins located under the CCD and far from hydrothermal sites. They were selected from Leg 129 (Karpoff, 1992) and Leg 199 (Pacific Ocean) (Lyle *et al.*, 2002) of the Ocean Drilling Program (ODP), and from Leg 73 (South Atlantic) of the Deep-Sea Drilling Program (DSDP) (Hsu *et al.*, 1984). In addition, a subsurface sediment rich in Fe-Mn hydroxide was collected at a water depth of 4.8 km from a Central Pacific abyssal hill, during the Valdiva VA13/2 cruise (Friedrich and Schmitz-Wiechowski, 1980). Specifically, 14 samples with sedimentary age of 0–11 Ma were chosen from Leg 129 Site 800 (21°55.38′N, 152°19.32′E), and from site Leg 199 site 1218 (8°53.378′N, 135°22.00′W) and Site 1219 (7°48.019′N, 142°00.940′W). Twenty-three samples with sedimentary age crossing the K-Pg boundary (~66 Ma) were chosen from ODP Leg 73 Site 524 (29°29.055′S, 3°30.74′E). Site 524 is located in the central part of the Cape Basin and is not influenced by the surface currents, nor by AABW and NADW currents. This site may be more influenced by Walvis ridge crustal materials (*e.g.*, titanomagnetite) essentially during the Maastrichtian.

Samples from these drill cores have already been extensively studied, in particular for mineralogy. All marine sediments selected for this study are characterized by abundant clay (>90% typically) and authigenic smectite (*e.g.* Hsu *et al.*, 1982, 1984). Moreover, we selected samples with only small amounts of calcite, illite and opal, thus minimizing the contribution from detrital component (dust) and biogenic phases.

We performed several tests to determine whether the sample pre-treatment may influence the lithium isotope composition (Table S-7). Tests were done on both bulk sediments and clay-sized fractions. For instance, clay-sized fractions (<2 μm) were extracted according to the Stokes Law and compared δ^7Li values obtained for bulk sediments. Possible influences of exchangeable cations, oxides and calcite could however be examined by comparing results for un-pretreated sediments (un-leached), and for samples leached with diluted nitric and acetic acid or exchanged with NH_4Cl. The 1N NaOH solution was also used to remove opal in three samples, which allowed us to verify the impact of biogenic phases. For the Leg 73 samples (K-Pg transition), clay fractions were systematically extracted and exchanged with NH_4Cl.

4. Li and δ^7Li Measurements

The detailed description of sample digestion and Li purification can be found in Vigier *et al.* (2008) and Bastian *et al.* (2017). Briefly, clay samples were digested with concentrated HF and HNO_3 acid. After re-dissolution in inverse aqua regia, the digested samples were dried down and dissolved in titrated 1M HCl. After complete dissolution is checked using centrifugation, a dual-step cation exchange chromatography protocol was used for Li elution and purification.

Elemental contents were measured by a VARIAN220 FS Atomic Absorption Spectrometer, with standard deviations ranging from 10% (<1 mg/l) to 1% (>100 mg/l) for Li in solution samples and ranging from 1% to 3% for Li in clay samples. Li isotope compositions of synthetic clays were analyzed using Multi Collector Inductively Coupled Plasma Mass Spectrometer (MC-ICP-MS, Neptune Plus) at ENS-Lyon (CNRS-INSU National platform of isotope analyses) and at UH Manoa (G&G department) following established procedures.

In this study, the uncertainties of reconstructed seawater δ^7Li values come from measurement, temperature reconstruction, and the coefficients of the $\Delta\delta^7$Li-T relationship. The propagation was performed in two main steps. First, the $\Delta\delta^7$Li-T relationship was obtained by weighted linear regression, where weights were based on the combined uncertainties of clay and solution measurements. The regression provided the fitted coefficients (slope and intercept) along with their covariance matrix, which accounts for their correlation. For any sample temperature, the uncertainty in $\Delta\delta^7$Li due to the coefficient errors was calculated from this covariance matrix. Separately, the 95% confidence interval of the reconstructed temperature was converted to a 1σ uncertainty and propagated through the temperature conversion and the linear relationship to yield an additional uncertainty component. These two independent contributions were then combined in quadrature to obtain the total uncertainty on $\Delta\delta^7$Li. Second, seawater δ^7Li is calculated as the measured clay δ^7Li minus $\Delta\delta^7$Li. The analytical uncertainty of the sample measurement was combined in quadrature with the total uncertainty on $\Delta\delta^7$Li to give the final uncertainty on reconstructed seawater δ^7Li.

5. Study of Crystal Chemistry

5.1. Synthetic clays

The crystallogenesis and the properties of smectites synthesized using the method described in section 1 have been previously extensively described (*e.g.*, Decarreau 1980, 1983). Notably, the actual incorporation of Li into the octahedral sheet of smectite has been demonstrated using ^{7}Li RMN spectroscopy: RMN spectra show a narrow single peak (less than 3 Gauss), which can undoubtedly be attributed to structural Li (Conard, 1975). The same synthesis procedure was also used to constrain chemical partitioning of M^{2+} cations (*e.g.* M=Fe, Ni, Co, Cu, Zn, or Mn) between Mg-smectites and water, and was found to be extremely reproducible (*e.g.*, Decarreau, 1985).

XRD patterns obtained on (1) powders and oriented preparations of synthesized NH_4-saturated Mg-Li-samples (without Al) in the air-dry state, (2) after ethylene glycol solvation and (3) after heating (300 °C, 4 hours) reveal that the produced solid phase contains only smectite, characterized by the basal reflections (001, 002, 003) and (hk) bands due to a turbostratic stacking of layers (Brindley and Brown, 1980). The (001) reflection (air-dry state) is at 11.2 Å, typical of NH_4^+saturated smectite. A d(06-33) distance of 1.52 Å is also usual for a Mg-Li trioctahedral smectite. After ethylene glycol solvation, harmonic (00l) reflections are observed at greater values (d(001)=16.8 Å) than those after air-drying, indicating an expansion of the smectite layers, due to the occurrence of a permanent interlayer charge. This supports Li for Mg octahedral hetero-valent substitution. After heating, the XRD patterns exhibit 001, 002, 003 reflections back to lower values (d(001)=9.8 Å), providing evidence for layer collapse, again confirming the synthesis of smectite. With the decrease of the synthesis temperature, the only change observed on the XRD patterns is peak broadening, due to a decrease of both the number of stacked layers and the dimension of crystal size within the layer plane, in smectite particles.

FTIR spectra (see Fig. S-3) of synthesized Mg-Li samples after NH_4^+ saturation confirm the synthesis of pure smectites at all temperatures in agreement with previous syntheses of Li-Mg smectites performed under similar conditions (Vigier *et al.*, 2008; Decarreau, 1980, 1983; Decarreau *et al.*, 2012), validating our synthesis protocol. The spectra exhibit a νNH_4 band near 1400 cm^{-1}, its absorbance being linked to the layer charge of the smectite (Petit *et al.*, 1998, 2006).

5.2. Marine clays crystal chemistry

5.2.1. Clay fractions from site 524 through the K-Pg transition. Samples from these drill cores have already been extensively studied, in particular for their mineralogy. Thus, all marine sediments selected for this study are characterized by abundant clay (>90% typically), primarily authigenic smectite (*e.g.* Hsu *et al.*, 1982, 1984). Moreover, we selected samples with the smallest amount of calcite, illite and opal, thus minimizing the contribution from detrital components (dust) and biogenic phases. This was further evidenced by the various chemical and sieving tests and measurements described in section 3 (results reported in Table S-3, S-4, S-5, S-6, S-7). We analyzed the structure and shape of bulk and clay fractions from leg 73 (site 524) using SEM and TEM (Philips EM300). TEM analyses of clay rich samples can also be found in Hsu *et al.* (1982, 1984). They reveal that Leg 73 samples contain mostly well-crystallized smectites of small-size, with thin and curled veils (Fig. S-4 and Fig. S-5). This is a typical shape of deep-sea smectites, considered to be authigenic, thus formed in situ. Indeed, in contrast, the detrital smectites are significantly bigger, denser, with no veils on the edges of particles, and are generally associated with other phyllosilicates such as illite, kaolinite, chlorite. Authigenic smectites have been found in other well-known K-Pg sites, as reviewed in Ortega-Huertas *et al.* (2002) and can form either from alteration of basaltic products and minerals or during an early-diagenetic process due to the dissolution of biogenic oozes (diatom frustules). XRD patterns and chemical compositions for the selected bulk samples reveal that the $CaCO_3$ content is very small as these sediments are mostly composed of clays - reddish brown clays - still included in a soft matrix. This sedimentology context is consistent with an oxidizing depositional environment below the CCD. Measured XRD patterns obtained for powders and oriented preparations of NH4-saturated samples (1) in the air-dry state, (2) after ethylene glycol solvation and (3) after heating (300 °C, 4 hours), as well as FTIR spectra, are shown below (Fig. S-6, Fig. S-7, Fig. S-8, Fig. S-9). Both techniques indicate that Site 524 clay fractions are essentially composed of smectite, with sometimes a few % of kaolinite. Using FTIR, we could observe first that the $CaCO_3$ observed in the bulk samples (Figure S-7) disappear in the clay fractions (Fig. S-8). All smectite-rich fractions are dioctahedral (2 octahedral sites over 3 are occupied by Al^{3+}, Fe^{3+} or Mg^{2+} cations) and therefore their diagenesis should result in their progressive transformation into illite. Some smectite particles display higher Al/Mg ratios because of small amounts of kaolinite or because of Al occupying tetrahedral sites. Incipient illitization of smectite (smectite-to-illite reaction) is indeed inferred from the presence of illite-smectite mixed-layers identified by XRD. However, it appears that the illitization process remains at a low level since observed smectite are only partly interstratified and still offer a large capacity of expansion during their treatment for XRD analyses. Altogether XRD and FTIR observations support the authigenic nature of these smectites and their small degree of diagenesis. Infrared

analyses (as referred in Russel and Fraser, 1994) reveal that there is a small amount of kaolinite in the Site 524 samples, which contain mostly Al-smectite.

5.2.2. Clay fractions from sites 1218 and 1219 and 800. All clay fractions from Sites 1218 and 1219 analyzed by XRD are smectite-rich (seen using Ethylen Glycol) with small amount of illite-smectite mixed-layers. They display the same level of diagenesis. SEM/EDS analyses show that smectite particles from Site 1218 look like chemically homogeneous flakes arranged in the form of tactoids, which are typical of marine authigenic smectites. No significant difference was observed in δ^7Li values among the various pre-treatments, confirming the negligible contribution from exchangeable Li or other phases (Table S-7). The age model was constructed using magnetochron boundaries as tie points throughout the entire studied interval. Calibrated ages for each magnetochron were initially assigned according to The Geologic Time Scale (2020). To ensure direct comparability with global reference datasets, the model was then linearly adjusted so that the K-Pg boundary corresponds to the widely accepted age of 66.04 Ma (Renne *et al.*, 2013). This normalization preserves the internal consistency of the model and does not affect the relative timing between magnetic reversals (Table S-8).

Supplementary Tables

Table S-1 Data and information corresponding to clay experimental syntheses.

Clay	T (°C)	Exp No	duration	saturation method*	LiCl initial	LiCl final solution					Saturated clay						$\Delta^7Li_{clay\text{-}solution}$ ‰	ref
						δ^7Li ‰	Err ‰	Li ppm	Si ppm	Mg ppm	δ^7Li ‰	Err ‰	SiO_2 %	Al_2O_3 %	MgO %	Li ppm		
sm	25	#1	4 weeks	(1)	3M (30ml)	15.2	0.1	20500	nd	nd	-4.8	0.2	50.7	0	22.9	81	-20.0	this study
sm	25	#2	8 weeks	(1)	3M(30ml)	15.2	0.1	20500	nd	nd	-5.1	0.5	50.4	0	22.9	88	-20.3	this study
sm	75	#1	16 weeks	(1)	0.25M (1ml)	15.4	0.1	18	13.7	39.7	-0.2	1.3	nd	0	18.9	34	-15.6	this study
sm	75	#2	16 weeks	(1)	0.25M (10ml)	14.2	0.2	186	14.3	41.2	-1.4	0.2	nd	0	18.5	124	-15.6	this study
sm	90	#1	16 weeks	(1)	0.25M (10ml)	15.9	0.2	192	28.1	41.1	1.5	0.2	nd	0	18.8		-14.5	this study
sm	150	#1	16 weeks	(1)	0.25M (0.33ml)	15.8	0.3	16	68	39	5.1	0.2	nd	0	23.5	165	-10.7	this study
sm	150	#2	16 weeks	(1)	0.25M (3.33ml)	15.7	0.2	186.0	64.7	45.8	5.7	0.2	nd	0	21.6	589	-10.0	this study
sm	200	#1	4 weeks	3xNH_4Cl	3M (30ml)	9.5	0.6	20500	nd	nd	6.1	1.0	nd	0	33.11	4348	-3.4	Vigier *et al.* 2008
sm	200	#2	4 weeks	3xNH_4Cl	3M (30ml)	9.5	0.6	20500	nd	nd	6.4	0.4	nd	0	27.49	3591	-3.1	Vigier *et al.* 2008
sm	200	#3	4 weeks	3xNH_4Cl	3M (30ml)	14.7	1.4	20500	nd	96	10.8	0.2	nd	0	26.50	3250	-3.9	Vigier *et al.* 2008
sm	250	#1	4 weeks	3xNH_4Cl	3M (30ml)	12.2	0.8	20500	nd	20.4	10.6	0.8	nd	0	27.65	3400	-1.6	Vigier *et al.* 2008
sm	250	#2	4 weeks	3xNH_4Cl	3M (30ml)	12.2	0.8	20500	nd	108.5	10.5	1.0	nd	0	27.60	3340	-1.7	Vigier *et al.* 2008
sm	250	#3	4 weeks	3xNH_4Cl	3M(30ml)	14.7	1.4	20500	nd	13.2	12.0	1.3	nd	0	nd	2707	-2.7	Vigier *et al.* 2008
kaol	200	#1	4 weeks	3xNH_4Cl	3M (30ml)	14.2	0.2	2980	218	39.6	10.9	0.2	52.8	30.6	0.01	2305	-3.3	this study
kaol	200	#2	4 weeks	3xNH_4Cl	3M (30ml)	14.5	0.1	3120	263	35.7	10.6	0.2	53.2	30.1	0.01	2185	-3.9	this study
Al-sm	200	#1	4 weeks	3xNH_4Cl	3M (30ml)	14.6	0.1	3265	42.0	0.37	11.0	0.1	58.9	21.8	2.36	3870	-3.6	this study
Al-sm	200	#2	4 weeks	3xNH_4Cl	3M (30ml)	14.8	0.2	3100	41.9	0.28	10.6	0.1	58.9	21.8	2.37	3795	-4.2	this study

*method (1) : 5 x $MgCl_2$, 3 x NH_4Cl

Table S-2 Data and information concerning Li-saturation and desorption experiments performed using SAZ Montmorillonite clay standard material.

name	sample type	Exp #	SiO_2	Al_2O_3	Fe_2O_3	MnO	MgO	CaO	Na_2O	K_2O	TiO_2	P_2O_5	LOI	Cs	Sr	Li	δ^7Li	err
			%	%	%	%	%	%	%	%	%	%	%	ppm	ppm	ppm	‰	‰
SAz-1 Montmorillonite																		
P1	Li-SAz #1 *	#1	62.8	18.2	1.6	0.1	6.3	0.1	< L.D.	0.16	0.24	0.03	11.1	25.9	11.9	6800	14.0	0.1
P2	Li-SAz #2 **	#2	62.3	18.2	1.6	0.1	6.2	0.1	0.1	0.15	0.24	0.03	10.7	8.1	12.8	6830	14.8	0.2
P4	(Cs, Li)-SAz #3 ***	#3	61.2	17.7	1.6	0.1	6.0	0.1	< L.D.	0.16	0.23	0.03	9.4	29360	13.1	5595	14.1	0.1
P3	Ca-SAz #4 ****	#4	61.3	17.9	1.6	0.1	6.5	3.0	0.1	0.22	0.23	0.03	9.7	10.7	349	205	-2.9	0.2
	published values *****		59.7	20.0	1.77		6.7	3.2	0.1	0.19	0.25	0.01	8.2	0.4	304			
Saturating Solutions																		
	1M LiCl after Li saturation	#1 & #2														6810	14.9	0.1
	1M LiCl after 1st Li saturation of Cs-SAz	#3												80		6710	14.2	0.3
	1M LiCl after 4th Li saturation of Cs-SAz	#3												11		6650	14.7	0.2
Desaturating solutions																		
	10^{-4}M LiCl after Li-SAz washing	#1														146	14.6	0.37
	H_2O after Li-SAz washing	#2														84	15.1	0.14

* After saturation with LiCl 1N, Li-SAz #1 was washed using 10^{-4}N LiCl

** After saturation with LiCl 1N, Li-SAz #2 was washed with water before washing, Li-SAz #1 and #2 were put in contact with the same 1N LiCl solution (in separate dialyze bags)

*** Here, Ca-SAz powder was first saturated with Cs (using a 0.01N CsCl solution), and then with Li (using 1N LiCl)

**** This SAz #4 aliquot was not saturated with Li but with Ca

***** Published concentrations measured in Ca-SAZ are from Mermut and Cano (2001) for major elements, Kogel and Lewis (2001) for trace elements

Table S-3 Compared chemical composition of bulk samples and clay fraction from site 524 across the K-Pg transition, highlighting clay dominance in the selected samples.

		SiO_2 (%)	Al_2O_3 (%)	Fe_2O_3 (%)	MnO (%)	MgO (%)	CaO (%)	Na_2O (%)	K_2O (%)	TiO_2 (%)
524-20-3, 105-106	Bulk	51.4	14.6	10.5	0.12	2.11	2.3	2.65	3.78	1.1
	<2µm	49.3	16.4	11.6	0.1	2.99	1.5	0.3	2.6	0.9
524-19-4 80-81	Bulk	53.1	16.6	11.0	0.06	3.10	< L.D.	0.12	2.77	0.9
524-21-1 129-130	Bulk	52.9	16.7	11.0	0.03	2.83	< L.D.	0.13	1.39	0.8
524-22-5 75-76	Bulk	56.5	15.9	10.1	0.04	3.24	< L.D.	0.11	1.40	0.8
524-27-2 136-137	Bulk	56.6	15.8	7.8	< L.D.	3.38	< L.D.	0.08	0.81	0.4
524-28-5 25-26	Bulk	55.3	14.1	11.2	0.05	3.63	< L.D.	0.15	3.53	0.8

Table S-4 Chemical composition and structural formula (basis 22 oxygens) of several smectites from site 524 through the K-Pg transition (#524 21 5 23-27) – XRD analyses of clay fraction.

	#524 21	#524 5	#524 23	#524 24	#524 25	#524 26	#524 27
SiO_2	55.76	52.72	51.87	51.96	51.62	42.20	53.23
Al_2O_3	16.32	15.52	15.25	15.14	15.11	12.09	15.86
MgO	3.50	3.27	3.21	3.27	3.22	2.38	3.43
Fe_2O_3	9.08	9.17	8.87	9.17	9.00	7.81	8.13
TiO_2	0.54	0.59	0.62	0.55	0.48	0.51	0.60
K_2O	1.09	1.07	1.07	1.05	0.99	1.25	1.40
CaO	1.36	1.41	1.40	1.34	1.29	1.02	1.48
Na_2O	0.37	0.35	0.37	0.38	0.38	0.26	0.59
Sum	88.02	84.10	82.66	82.86	82.09	67.52	84.72
Si	7.71	7.65	7.66	7.66	7.67	7.67	7.67
AlIV	0.29	0.35	0.34	0.34	0.33	0.33	0.33
AlVI	2.37	2.31	2.31	2.29	2.32	2.26	2.36
Fe^{3+}	0.94	1.00	0.99	1.02	1.01	1.07	0.88
Mg	0.72	0.71	0.71	0.72	0.71	0.64	0.74
Ti	0.06	0.06	0.07	0.06	0.05	0.07	0.06
K	0.19	0.20	0.20	0.20	0.19	0.29	0.26
Ca	0.20	0.22	0.22	0.21	0.21	0.20	0.23
Na	0.10	0.10	0.11	0.11	0.11	0.09	0.16
Int Ch.	0.69	0.74	0.75	0.73	0.71	0.78	0.88
Oct. Occ.	4.09	4.08	4.08	4.09	4.09	4.04	4.04

All compositions are close to typical montmorillonite (Si: 8.00; Al^{IV}: 0.00; Al^{VI}: 3.34; Mg: 0.71), compared to beidellite or nontronite, which contain no Mg, more Al^{IV} and Al^{VI} (Beidellite) or much more Fe^{3+} (Nontronite).

Table S-5 Published mineralogical proportions made by LAS (*) or by XRD (+) (Vanden Berg and Jarrard, 2006; Karpoff, 1992).

Sample	smectite %	illite %	calcite %	opal %
1218A-1H-6-25-26+	>90			
1219A-1H-2-122-123*	96.7	0.0	3.3	0.0
1219A-1H-3-73-74*	100.0	0.0	0.0	0.0
1219A-1H-4-25-26*	84.8	0.0	0.0	15.2
1219A-1H-4-61-62*	93.9	0.0	0.0	6.1
1218A-3H-1-78-79*	73	0	0	27
800-4R-01-97+	>90			

Table S-6 Compared chemical composition of samples from site 1218, 1219 and 522, highlighting the dominance of clay

	SiO_2 %	Al_2O_3 %	Fe_2O_3 %	MnO %	MgO %	CaO %	Na_2O %	K_2O %	TiO_2 %
Valvidia VA13/2 96BL	54.62	12.95	10.49	1.28	4.34	0.24	0.31	1.30	0.47
1219A-1H-3W-122-123	55.26	13.84	8.65	0.64	3.71	0.27	0.38	1.66	0.62
1218B-3H-3W-85-86	54.84	13.53	9.00	0.57	3.37	0.27	0.40	1.87	0.62
522-9H-2W-134-140	48.74	16.39	12.14	1.57	3.06	0.13	0.35	2.94	0.66
1218A-5H-3W-24-25	53.57	9.91	13.48	1.54	3.30	0.31	0.34	1.72	0.50

Table S-7 Li isotopic compositions of marine clays collected from the Pacific and the Atlantic Ocean

Sample	Age Ma	δ^7Li ‰	Li ppm	T* °C	pretreatment
Valvidia VA13/2 96BL	0	5.2	136.6	3.0	clay-size extraction (rich in Fe-Mn nodules)
	rep	6.0	159.1	3.0	clay-size extraction (rich in Fe-Mn nodules)
1218A-1H-6-25-26	1.75	5.0		1.9	bulk sediment pretreated with 0.2M HNO_3
	rep	4.7	63.9	1.9	bulk sediment pretreated with 0.2M HNO_3 and then 1M NaOH
1219A-1H-2-122-123	2.35	5.7	96.3	1.9	bulk sediment pretreated with 0.2M HNO_3
	rep	5.6		1.9	bulk sediment pretreated with 0.2M HNO_3
	rep	5.3	91.7	1.9	clay-size extraction pre-treated with 0.2M HNO_3
1219A-1H-3-73-74	3.22	5.4	94.0	3.7	bulk sediments
	rep	6.0	102.4	3.7	bulk sediments
	rep	5.7	87.8	3.7	bulk sediment pretreated with 0.2M HNO_3
	rep	5.8	87.3	3.7	bulk sediments
	rep	5.9	87.3	3.7	bulk sediments
1219A-1H-3W-122-123	3.62	6.0	104.9	4.1	clay-size extraction
1219A-1H-4-25-26	4.08	6.0	92.3	4.5	bulk sediment pretreated with 0.2M HNO_3
	rep	5.6	81.8	4.5	bulk sediment pretreated with 0.2M HNO_3 and then 1M NaOH
1219A-1H-4-61-62	4.39	5.9	87.4	4.7	bulk sediment pretreated with 0.2M HNO_3
	rep	5.6	105.1	4.7	bulk sediment pretreated with 0.2M HNO_3 and then 1M NaOH
1219A-1H-4-76-77	4.50	5.3		4.7	clay-size fraction
	rep	5.0		4.7	clay-size fraction pretreated with NH_4Cl
1218A-3H-1-78-79	4.81	5.3	65.7	4.9	bulk sediments
	rep	5.0	69.7	4.9	bulk sediment pretreated with 0.2M HNO_3

1218B-3H-3W-45-46	5.93	5.0	85.6	5.3	clay-size extraction
1218B-3H-3W-85-86	6.09	4.9	79.9	5.4	clay-size extraction
1218B-3H-5W-68-69	6.90	5.1	81.1	5.6	clay-size extraction
1218B-3H-5W-115-116	6.97	4.8	88.6	5.7	clay-size extraction
1219A-2H-4W-76-77	9.87	5.3	129.5	7.5	clay-size extraction
800-4R-01-97	10.6	4.1	52.0	8.0	clay-size extraction
	rep	3.9		8.0	clay-size extraction and diluted HAc leaching
	rep	4.4		8.0	clay-size extraction and diluted HAc-HNO_3 leaching
73-522-9H-2W-134-140	10.14	3.4	59.5	7.7	clay-size extraction
73-522-9H-CC	10.50	3.4	60.3	8.0	clay-size extraction

Table S-8 Age model used for Leg 73 Site 524.

Average Depth [m]	Depth top [m]	Depth bottom [m]	Label 1 (top)	Label 2 (bottom)	Chron transition	Reference for GTS 2020	Age from GTS 2020 [kyr]
58.22	58.11	58.32	73-524-5R-1,111	73-524-5R-1,132	C24/C25	topc25n	57101
129.04	128.84	129.23	73-524-12R-4,84	73-524-12R-4,123	C26/C27	topc27n	62278
156.45	156.26	156.64	73-524-15R-3,126	73-524-15R-4,14	C27/C28	topc28n	63537
185.29	185.10	185.48	73-524-18R-4,10	73-524-18R-4,48	C28/C29	topc29n	64862
200.30	200.08	200.50				topc29r	65700
213.37	213.02	213.72	73-524-21R-3,102	73-524-21R-4,22	C29/C30	topc30n	66380
267.56	267.31	267.81	73-524-27R-1,131	73-524-27R-2,31	C30/C31	topc31n	68351
303.94	303.93	303.94	73-524-32R-1,43	73-524-32R-1,44	C31N/C31R	topc31r	69271

Table S-9 Temperature calibrations, Li isotope fractionation factors, and reconstructed seawater δ^7Li for Site 524 samples (GTS2020 ages).

Table S-9 (xlsx) is available for downloading from the online version of this article at https://doi.org/10.7185/geochemlet.2628.

Supplementary Figures

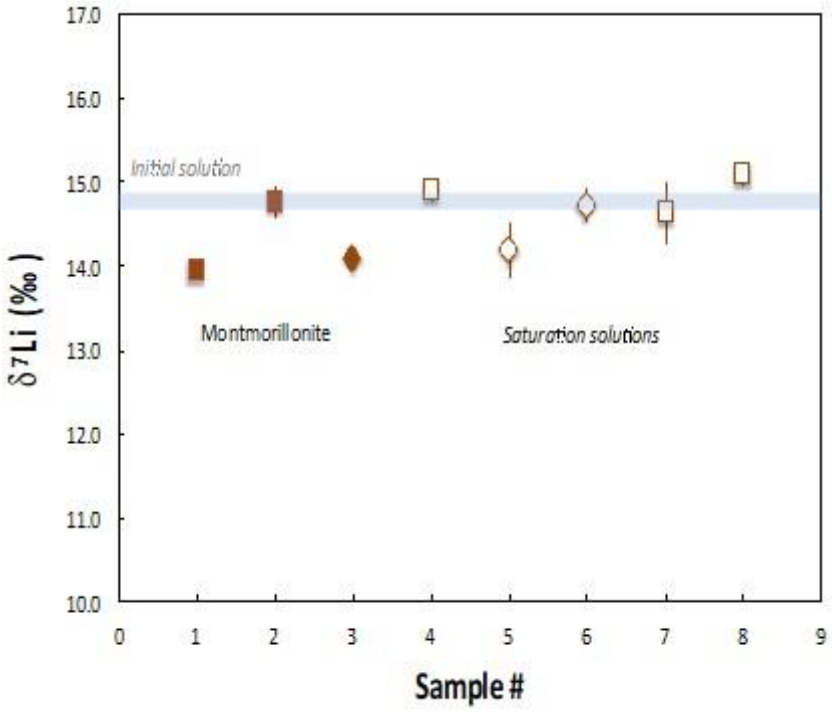

Figure S-1 Results for Li desorption/adsorption experiments. Full symbols: Montmorillonite saturated with Li (squares) or with Cs and Li (diamonds). Open symbols: solutions used for the saturation experiments. The δ^7Li value of the unsaturated montmorillonite is – 2.9‰. The values measured for both the montmorillonite saturated with Li, for the Li solutions collected after desorption, and the initial Li solution are similar within uncertainties (±0.5‰) indicating a negligible isotopic fractionation caused by adsorption and desorption.

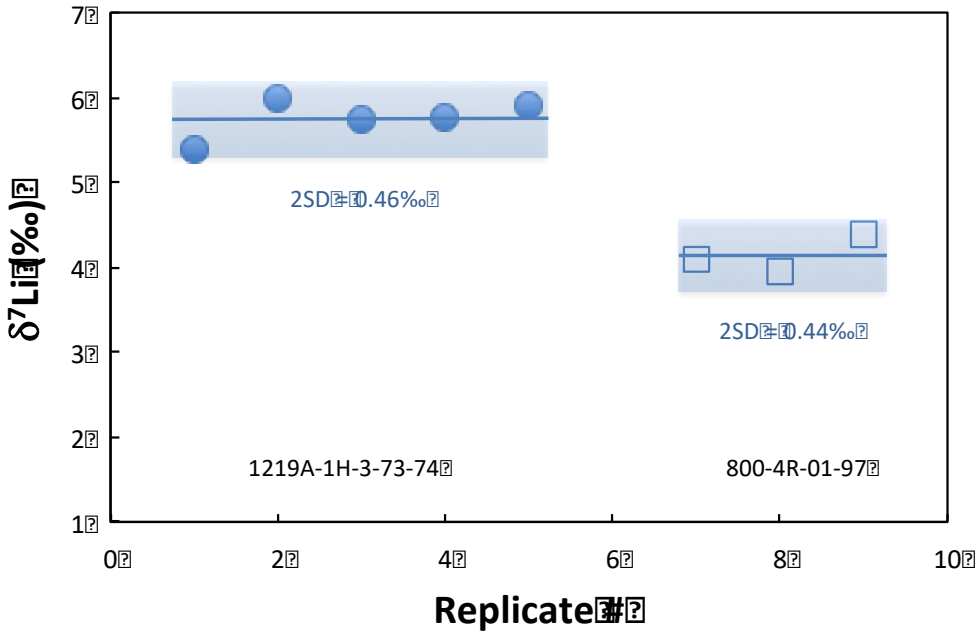

Figure S-2 example of reproducibility for marine clays δ^7Li values. Additional results can be found in Table S-7. Each symbol represents a distinct clay fraction extracted from the same age sediment. The external reproducibility is about 0.4 ‰ at the 2σ level.

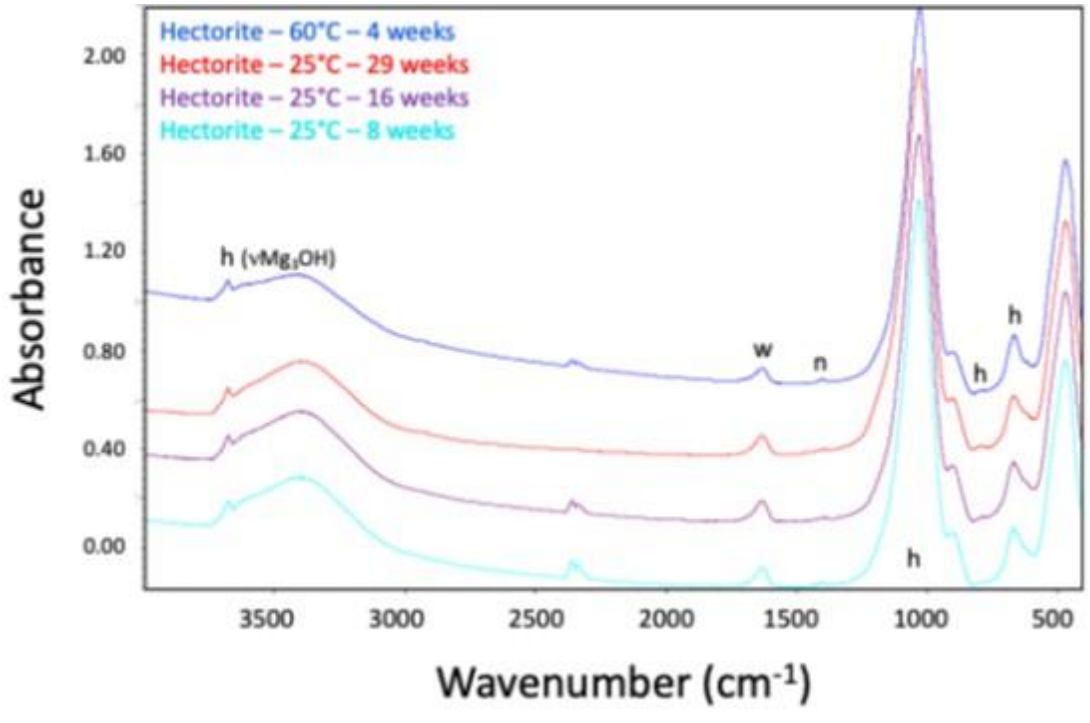

Figure S-3 FTIR analyses of clays synthesized at low temperature highlighting the dominance of hectorite (h): no peak is consistent with kaolinite, chlorite nor illite. Note that w = water, and n = NH_4.

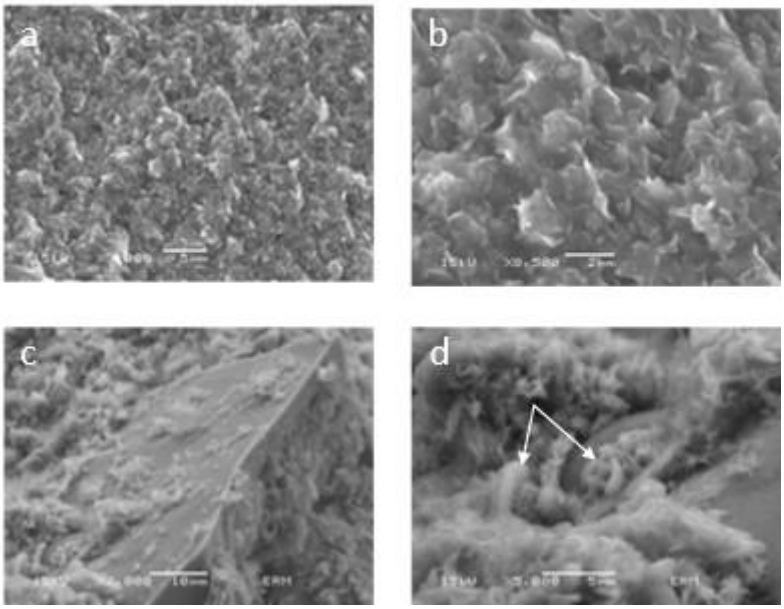

Figure S-4 SEM photographs of clay fraction from site 524 at the K-Pg transition. a) and b): 524 21 5 23-27; c) and d): 524 21R 1 129-130. Authigenic smectite can form from alteration of basaltic products or by dissolution of biogenic ooze including diatom frustules (white arrows).

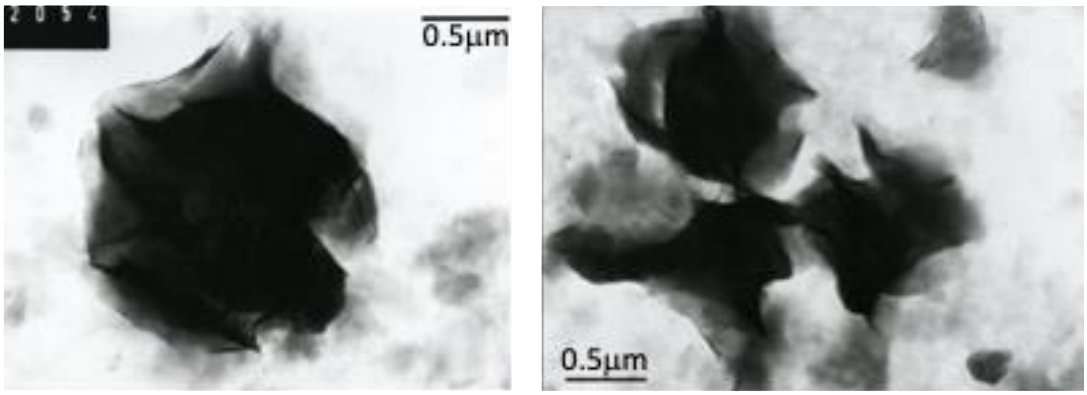

Figure S-5 TEM analysis of reddish-brown clays typically observed at Leg 73, site 524, across the K-Pg transition, below and above the Ir-rich layer. Sample #524 21-5 11-13 is shown here as an illustration. We can see well preserved smectite particles of small size with thin and curled veils, which is a typical shape of deep sea smectites considered as authigenic.

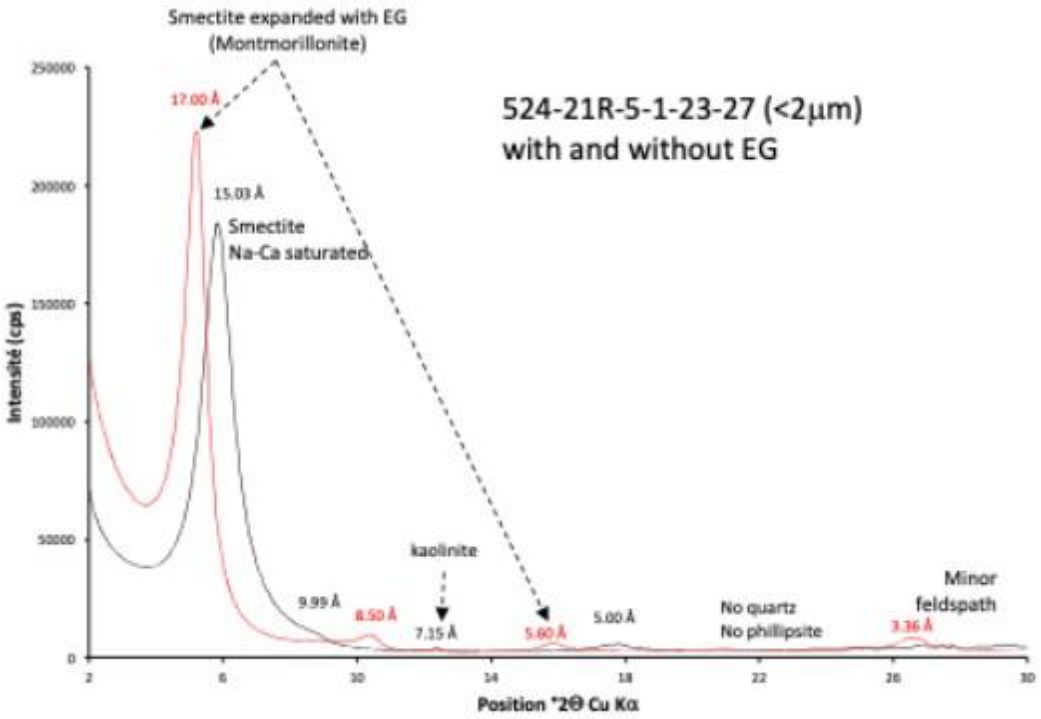

Figure S-6 XRD analysis of clay fraction from sample 524 21 5 23-27. The treatment with Ethylene Glycol (EG) (red line) demonstrates that the dominant phase is a pure smectite (montmorillonite), without any interstratification of non-expanded layers. No illitization is visible, supporting the very low degree of diagenesis. Black line shows the same sample without EG treatment.

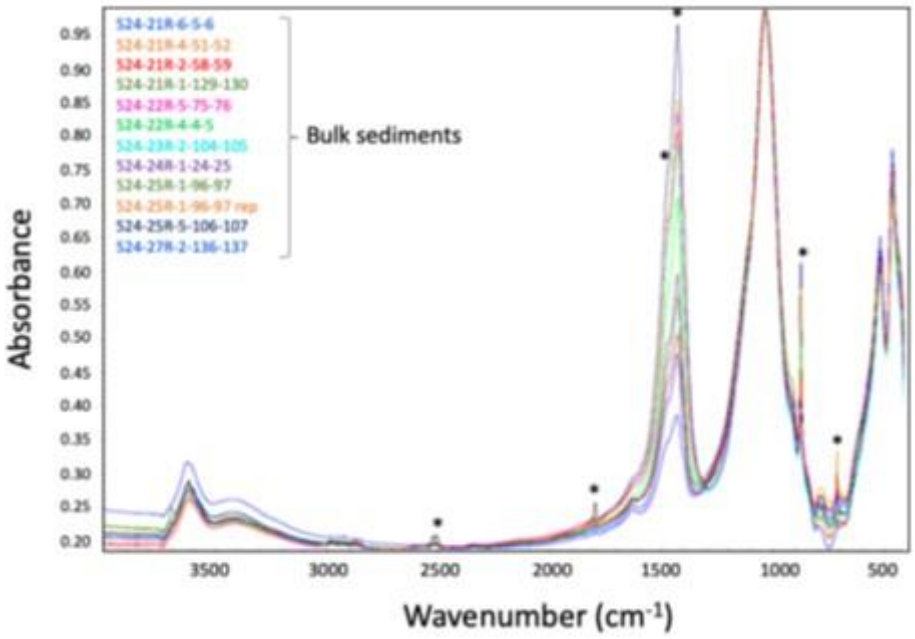

Figure S-7 FTIR analyses of smectite-rich dried bulk samples from site 524 over the K-Pg transition. Stars indicate calcite peaks.

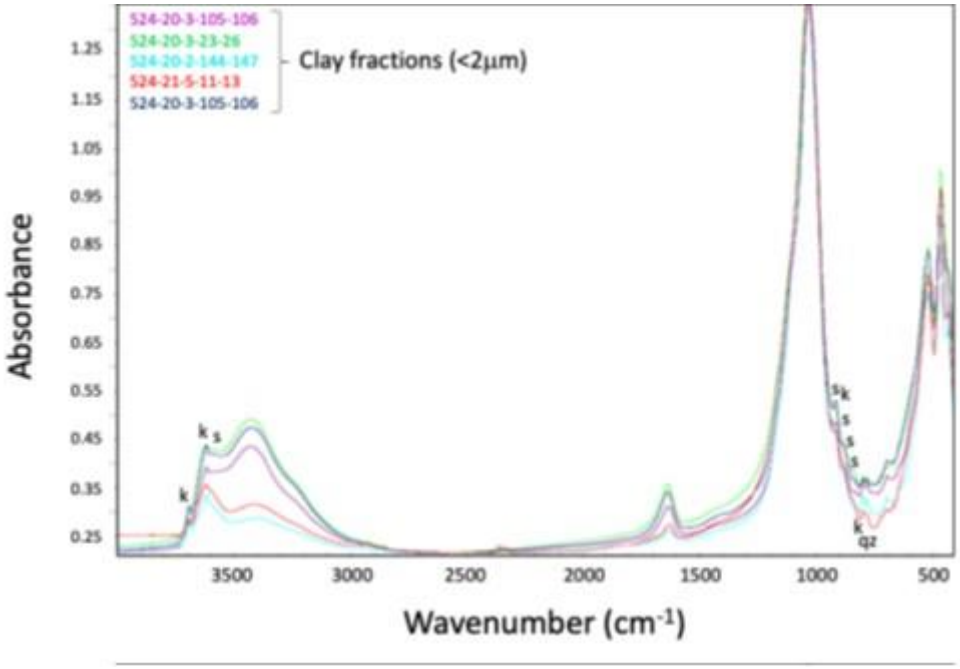

Figure S-8 FTIR analyses of dried clay fraction (<2um) extracted from site 524 over the K-Pg transition. s: smectite; k: kaolinite; qz: quartz. Note that the relative absorbance is higher for kaolinite compared to smectite since less than 1% of kaolinite in mixture with smectite can be revealed by FTIR (Joussein *et al.*, 2001).

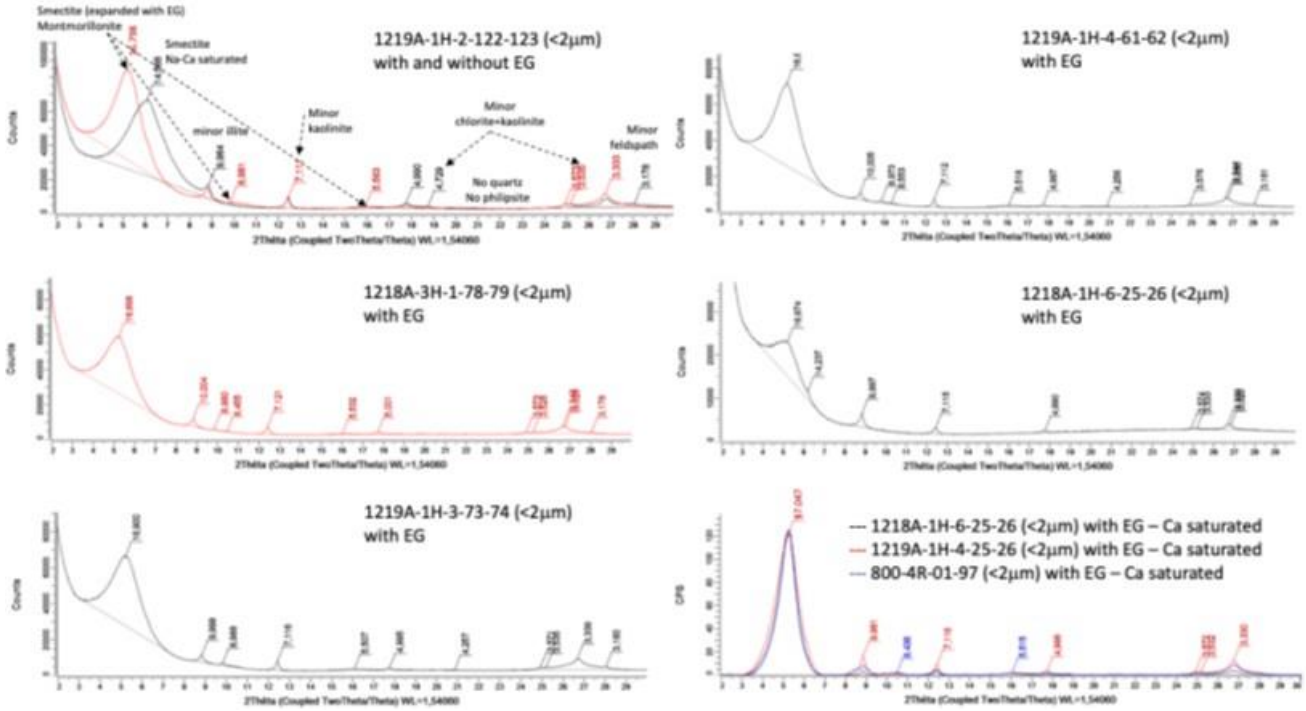

Figure S-9 XRD analyses of clay fractions from the different sits selected for the 0-15Myr period (see Table S-3). EG: Ethylene Glycol. All clay fractions show similar patterns with a dominance of montmorillonite (expanding under EG treatment), and minor phases such as illite, kaolinite or feldspaths. The expansion capacity of the smectite, and the symmetric and fine shape of their peak under EG (when Ca-saturated) indicate low level of diagenesis and good crystallinity.

Supplementary Information References

Barnet, J.S.K., Littler, K., Westerhold, T., Kroon, D., Leng, M.J., Bailey, I., Röhl, U., Zachos, J.C. (2019) A High-Fidelity Benthic Stable Isotope Record of Late Cretaceous–Early Eocene Climate Change and Carbon-Cycling. *Paleoceanography and Paleoclimatology* 34, 672-691. https://doi.org/10.1029/2019PA003556

Bastian, L., Revel, M., Bayon, G., Dufour, A., Vigier, N. (2017) Abrupt response of chemical weathering to Late Quaternary hydroclimate changes in northeast Africa. *Scientific Reports* 7, 44231. https://doi.org/10.1038/srep44231.

Brindley, G.W., Brown, G. (1980) *Crystal Structures of Clay Minerals and Their X-ray Identification*. Mineralogical Society, London.

Conard, J. (1975) Étude structurale de l'eau adsorbée sur l'hectorite-Li par RMN de 1H et 7Li. In: Bailey, S.W. (Ed.) *Proceedings of the International Clay Conference, 1975*. Applied Publishing Ltd., 221–230.

Dameron, S.N., Leckie, R.M., Clark, K., MacLeod, K.G., Thomas, D.J., Lees, J.A. (2017) Extinction, dissolution, and possible ocean acidification prior to the Cretaceous/Paleogene (K/Pg) boundary in the tropical Pacific. *Palaeogeography, Palaeoclimatology, Palaeoecology* 485, 433-454. https://doi.org/10.1016/j.palaeo.2017.06.032.

Decarreau, A. (1980) Cristallogenèse expérimentale des smectites magnésiennes: hectorite, stevensite. *Bulletin de Minéralogie* 103, 579–590.

Decarreau, A. (1983) Étude expérimentale de la cristallogenèse des smectites. Mesures des coefficients de partage smectite trioctaédrique-solution aqueuse pour les métaux M2+ de la première série de transition. *Sciences Géologiques* 74, 190.

Decarreau, A. (1985) Partitioning of transition elements between octahedral sheets of trioctahedral smectites and water. *Geochimica et Cosmochimica Acta* 49, 1537–1544. https://doi.org/10.1016/0016-7037(85)90258-3.

Decarreau, A., Vigier, N., Palkova, H., Petit, S., Vieillard, P., Fontaine, C. (2012) Partitioning of lithium between smectite and solution: An experimental approach. *Geochimica et Cosmochimica Acta* 85, 314–325. https://doi.org/10.1016/j.gca.2012.02.020.

Friedrich, G., Schmitz-Wiechowski, A. (1980) Mineralogy and chemistry of a ferromanganese crust from a deep-sea hill, central Pacific, "Valdivia" cruise VA 132. *Marine Geology* 37, 71–90. https://doi.org/10.1016/0025-3227(80)90047-2.

Fischer, A., Batenburg, S.J., Bahr, A., Voigt, S., Rheinberger, A., Schmickal, S., Rheinberger, S., Greule, M., Rheinberger, S., Friedrich, O. (2025) Precession-paced late Maastrichtian bottom-water dynamics. *Communications Earth and Environment* 6, 239. https://doi.org/10.1038/s43247-025-02219-y.

Hsü, K.J., He, Q., McKenzie, J.A., Weissert, H., Perch-Nielsen, K., Oberhänsli, H., Kelts, K., Labrecque, J., Tauxe, L., Krähenbühl, U., Percival, S.F. Jr., Wright, R., Karpoff, A.M., Petersen, N., Tucker, P., Poore, R.Z., Gombos, A.M., Pisciotto, K., Carman, M.F. Jr., Schreiber, E. (1982) Mass mortality and its environmental and evolutionary consequences. *Science* 216, 249–256. https://doi.org/10.1126/science.216.4543.249.

Hsü, K.J., Labrecque, J.L., *et al.* (Shipboard Scientific Party, Leg 73) (1984) Sites reports: Sites 519, 520, 521, 522, 523 and 524. *Initial Reports of the Deep Sea Drilling Project* 73, 27–383.

Joussein, E., Petit, S., Decarreau, A. (2001) Une nouvelle méthode de dosage des minéraux argileux en mélange par spectroscopie IR. *Comptes Rendus de l'Académie des Sciences* 332, 83–89. https://doi.org/10.1016/S1251-8050(00)01495-X.

Karpoff, A.M. (1992) Cenozoic and Mesozoic sediments from the Pigafetta Basin, Leg 129, Sites 800 and 801: Mineralogical and geochemical trends of the deposits overlying the oldest oceanic crust. *Proceedings of the Ocean Drilling Program, Scientific Results* 129, 3–30.

Kogel, J.E., Lewis, S.A. (2001) Baseline studies of The Clay Minerals Society Source Clays: Chemical analyses by inductively coupled plasma mass spectroscopy (ICP-MS). *Clays and Clay Minerals* 49, 387–392. https://doi.org/10.1346/CCMN.2001.0490504.

Lyle, M., Wilson, P.A., Janecek, T.R., *et al*. (2002) *Proceedings of the Ocean Drilling Program, Initial Reports*, 199. Ocean Drilling Program, College Station, TX.

Meckler, A.N., Sexton, P.F., Piasecki, A.M., Leutert, T.J., Marquardt, J., Ziegler, M., *et al*. (2022) Cenozoic evolution of deep ocean temperature from clumped isotope thermometry. *Science* 377, 86–90. https://doi.org/10.1126/science.abk0604.

Mermut, A., Cano, A.F. (2001) Baseline studies of The Clay Minerals Society Source Clays: Chemical analyses of major elements. *Clays and Clay Minerals* 49, 381–386. https://doi.org/10.1346/CCMN.2001.0490503.

Ortega-Huertas, M., Martínez-Ruiz, F., Palomo, I., Chamley, H. (2002) Review of the mineralogy of the Cretaceous-Tertiary boundary clay: Evidence supporting a major extraterrestrial catastrophic event. *Clay Minerals* 37, 395–411. https://doi.org/10.1180/0009855023730055.

Petit, S., Righi, D., Madejova, I., Decarreau, A. (1998) Layer charge of smectites: Quantification and localization using infrared spectroscopy. *Clay Minerals* 33, 579–591. https://doi.org/10.1180/000985598545647.

Petit, S., Righi, D., Madejová, J. (2006) Infrared spectroscopy of NH4-bearing and saturated clay minerals: A review of the study of layer charge. *Applied Clay Science* 34, 22–30. https://doi.org/10.1016/j.clay.2006.08.001.

Renne, P.R., Deino, A.L., Hilgen, F.J., Kuiper, K.F., Mark, D.F., Mitchell, W.S., *et al*. (2013) Time scales of critical events around the Cretaceous-Paleogene boundary. *Science* 339, 684–687. https://doi.org/10.1126/science.1230492.

Russell, J.D., Fraser, A.R. (1994) Infrared methods. In: Wilson, M.J. (Ed.) *Clay Mineralogy: Spectroscopic and Chemical Determinative Methods*. Chapman & Hall, London, 11–67.

Vanden Berg, M.D., Jarrard, R.D. (2006) Data report: High-resolution mineralogy for Leg 199 based on reflectance spectroscopy and physical properties. In: Wilson, P.A., Lyle, M., Firth, J.V. (Eds.) *Proceedings of the Ocean Drilling Program, Scientific Results* 199, 1–23.

Vigier, N., Decarreau, A., Millot, R., Carignan, J., Petit, S., France-Lanord, C. (2008) Quantifying Li isotope fractionation during smectite formation and implications for the Li cycle. *Geochimica et Cosmochimica Acta* 72, 780–792. https://doi.org/10.1016/j.gca.2007.11.011.